Proceedings of ASME Turbo Expo 2011
GT2011
June 6-10, 2011, Vancouver, British Columbia, Canada

GT2011-45310

EXPERIMENTAL MEASUREMENTS OF INGESTION THROUGH TURBINE RIM SEALS.

PART 1: EXTERNALLY-INDUCED INGRESS

Carl M Sangan, **Oliver J Pountney**, **Kunyuan Zhou***, **Mike Wilson**, **J Michael Owen**, **Gary D Lock**

Dept. of Mechanical Engineering
University of Bath
Bath, BA2 7AY
United Kingdom

* Dept. of Engineering Thermophysics
School of Jet Propulsion
Beihang University
Beijing, 100191 P.R.China

ABSTRACT

This paper describes a new research facility which experimentally models hot gas ingestion into the wheel-space of an axial turbine stage. Measurements of CO_2 gas concentration in the rim-seal region and inside the cavity are used to assess the performance of two generic (though engine-representative) rim-seal geometries in terms of the variation of concentration effectiveness with sealing flow rate. The variation of pressure in the turbine annulus, which governs this externally-induced (EI) ingestion, was obtained from steady pressure measurements downstream of the vanes and near the rim seal upstream of the rotating blades.

Although the ingestion through the rim seal is a consequence of an unsteady, three-dimensional flow field and the cause-effect relationship between pressure and the sealing effectiveness is complex, the experimental data is shown to be successfully calculated by simple effectiveness equations developed from a previously published orifice model. The data illustrate that, for similar turbine-stage velocity triangles, the effectiveness can be correlated using a non-dimensional sealing parameter, Φ_o. In principle, and within the limits of dimensional similitude, these correlations should apply to a geometrically-similar engine at the same operating conditions.

Part 2 of this paper describes an experimental investigation of rotationally-induced (RI) ingress, where there is no main-steam flow and consequently no circumferential variation of external pressure.

NOMENCLATURE

a	speed of sound
b	radius of seal
c	concentration
C	velocity relative to vane
$C_{d,e}$ $C_{d,i}$	discharge coefficients for egress, ingress
C_p	pressure coefficient [$= (p_2 - \overline{p_2}) / (^1/_2\, \rho\Omega^2 b^2)$]
$C_{p,max}$	pressure coefficient [$= \Delta p / (^1/_2\, \rho W^2)$]
C_w	non-dimensional flow rate [$= \dot{m} / \mu b$]
$C_{w,e}$, $C_{w,i}$	values of C_w for egress, ingress
$C_{w,o}$	non-dimensional sealing flow rate
$C_{w,min}$	minimum value of $C_{w,o}$ to prevent ingress
G_c	seal-clearance ratio [$= s_c / b$]
K	empirical constant
$\dot{m}$	mass flow rate
M	Mach number
p	absolute static pressure
$\overline{p}$	mean absolute static pressure over one vane pitch
r	radius
Re_w	axial Reynolds number in annulus [$= \rho W b / \mu$]
Re_ϕ	rotational Reynolds number [$= \rho\Omega b^2 / \mu$]
s	axial clearance between rotor and stator
s_c	seal clearance
$s_{c,o}$	radial-seal clearance for stationary case
U	bulk mean velocity of sealing flow [$= \dot{m}_o / 2\pi\rho b s_c$]
V	velocity relative to blade
V_ϕ	tangential component of velocity
W	axial velocity in annulus
ΔC_p	non-dimensional pressure difference [$= \Delta p / (^1/_2\, \rho\Omega^2 b^2)$]
Δp	peak-to-trough pressure difference in annulus [$= p_{2,max} - p_{2,min}$]
α	vane angle
β	blade relative angle
β_o	blade relative angle at design
Γ_c	ratio of discharge coefficients [$= C_{d,i} / C_{d,e}$]
δ	radial growth of seal
ε	sealing effectiveness [$= C_{w,0} / C_{w,e} = \Phi_0 / \Phi_e$]

ε_c concentration effectiveness [$= (c_s\text{-}c_a) / (c_o\text{-}c_a)$]

Φ non-dimensional sealing parameter [$= C_w / 2\pi G_c Re_\Phi$]

Φ_i value of Φ when $C_w = C_{w,i}$

Φ_i* value of Φ_i when $\Phi_0 = 0$

Φ_{min} value of Φ when $C_w = C_{w,min}$

Φ_0 value of Φ when $C_w = C_{w,0}$

θ angular coordinate, non-dimensional vane pitch

λ_T turbulent flow parameter [$= C_{w,o} Re_\phi^{-0.8}$]

μ dynamic viscosity

ρ density

σ standard deviation

Ω angular velocity of rotating disc

Subscripts

a annulus

ax axial-clearance seal

e egress

EI externally-induced ingress

i ingress

max maximum

min minimum

o superposed flow, zero rotation

rad radial-clearance seal

RI rotationally-induced ingress

s stator

1,2 locations in wheel-space and annulus

* value when $C_{w,o}=0$

1. INTRODUCTION

The internal air system of a gas turbine distributes the air extracted from the main-gas path at several axial locations in the compressors. This secondary flow of air is used to ventilate and cool the engine components, and to balance the pressure distribution on the rotating discs in order to maintain acceptable bearing loads. Fig. 1a illustrates a typical high-pressure gas-turbine stage where cooling air limits the metal temperatures to ensure the integrity and operating life of the blade and vanes.

Another important function of the secondary air system is to reduce the ingestion of hot mainstream gas through rim seals at the vane and blade platforms (see Fig. 1b) and this is achieved by supplying a sealing (sometimes called purge) flow of pressurised air into the wheel-space (or disc cavity) between the stator and rotor. This sealing air also acts to maintain tolerable under-platform and disc metal temperatures. The flow is expelled from the wheel-space into the main gas-path annulus through the gap in the rim seal.

The diversion of compressed air and its subsequent mixing with the main-gas flow exact penalties on the performance of the machine, and so the engine designer wishes to accomplish the tasks of sealing the cavity and cooling the metal with a minimum of mass flow.

The flow past the stationary vanes and rotating blades in the turbine annulus creates an unsteady 3D variation of pressure radially outward of the rim seal, as illustrated in Fig. 2. The effective time-average peak-to-trough pressure difference comprises separate components produced by the vanes and blades, and these effects attenuate with distance from the trailing and leading edges respectively.

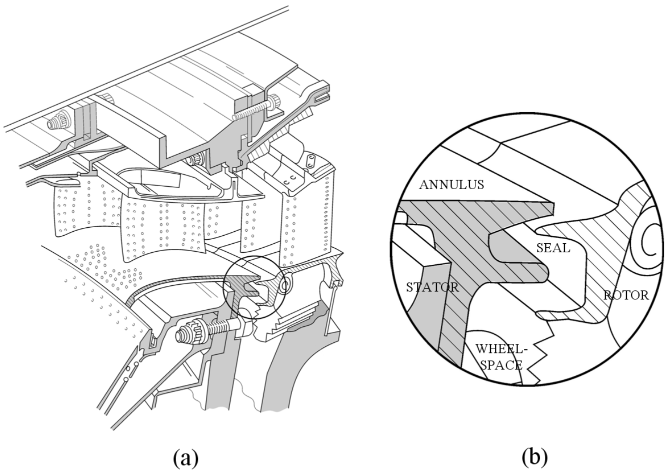

Fig. 1: (a) Typical high-pressure gas-turbine stage; (b) detail of rim seal

Ingress and egress occur through those parts of the seal clearance where the external pressure is higher (marked + in Fig. 2) and lower (marked -), respectively, than that in the wheel-space. This non-axisymmetric type of ingestion is the dominant mechanism of ingress in gas turbines and Owen [1, 2] defined this as *externally-induced* (EI) ingress.

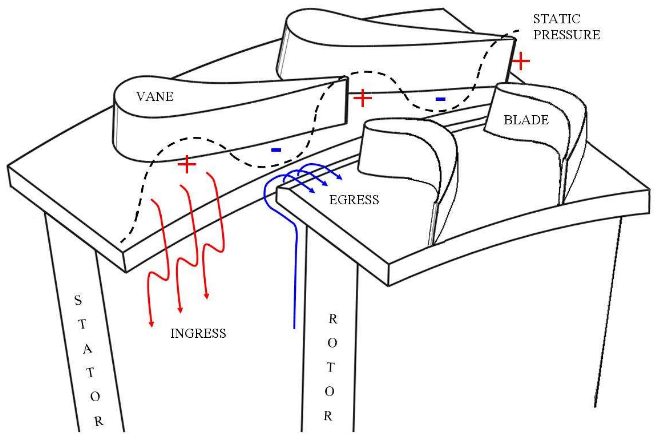

Fig. 2: Variation of static pressure in a turbine annulus. Red arrows indicate hot-gas ingress and blue cooler egress; corresponding to regions of high and low pressure with respect to the wheel-space, respectively

Numerous factors influence the degree of ingestion into the wheel-space: the vane and blade geometries and their axial spacing; the Mach and Reynolds numbers of the flow in the annulus; the configuration of the rim seal and its location relative to the vanes and blades; and the non-dimensional sealing flow parameter, Φ_o. This last variable is defined in the nomenclature and is discussed further below.

Fig. 3a shows a simplified diagram of ingress and egress through an axial-clearance rim seal. Cool sealing air enters the wheel-space and fills a source region at low radius. This flow is entrained into the boundary layer on the rotating disc, which thickens with increasing radius, before it is ejected into the turbine annulus.

There is a mixing region near the outer radius of the cavity, where hot gas ingested from the annulus mixes with the recirculating flow in the wheel-space. The ingested gas is transported in the boundary layer on the stator which (in contrast to that on the rotor) loses mass as the fluid moves radially inwards over the stator surface. Thus there is axial migration of fluid, through a core region, from the stator to the rotor boundary layer. Consequently the average temperature of the rotor boundary layer increases with radius but the temperature on the stator is approximately constant. The core region is diminished in size, and pushed to higher radius (see Fig. 3b), as the superimposed sealing flow rate increases to Φ_{min}, the value of Φ_o necessary to prevent ingress.

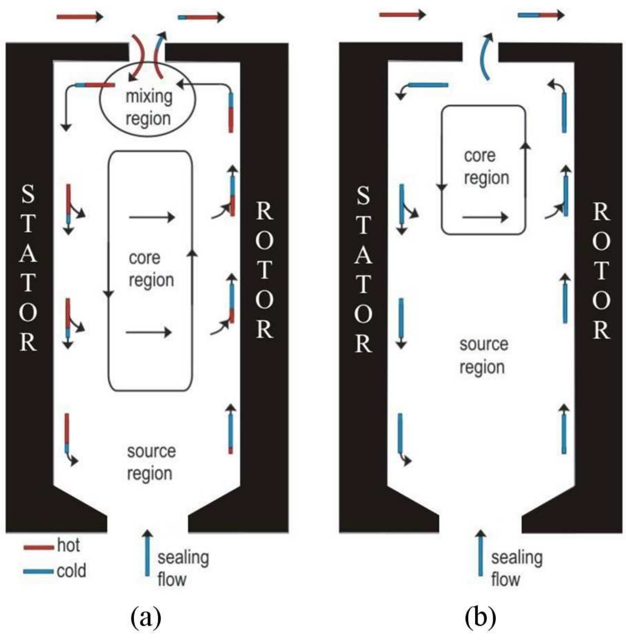

Fig. 3: Simplified diagram of ingress and egress (a) $\Phi_0 < \Phi_{min}$ (b) $\Phi_0 = \Phi_{min}$

Although the sealing air can reduce ingress, too much air reduces the engine efficiency and too little can cause serious overheating, resulting in damage to the turbine rim and blade roots. In terms of internal air systems, the engine designer wants to know the following: the most effective seal geometry; how much sealing air is required to limit ingestion to an acceptable level; when ingress occurs, how much hot gas enters the wheel-space; how does this ingested fluid affect the temperatures on the rotating and stationary components.

This paper describes a new experimental facility which models hot gas ingestion into the wheel-space of an axial turbine stage. Measurements of CO_2 gas concentration in the rim seal region and inside the wheel-space were used to determine the variation of ε_c, the sealing effectiveness based on concentration, with Φ_o. The variation of pressure in the annulus, which governs the externally-induced ingestion, was obtained from steady pressure measurements on the platform downstream of the vanes and at the outer casing near the rim seal. The investigation assesses the performance of two generic (though engine-representative) rim-seal geometries in terms of this sealing effectiveness.

The measurements provide a database to validate CFD codes and provide insight into the physical phenomena governing hot gas ingestion. Furthermore, the effectiveness equations, developed from orifice models for ingress described in Part 2 of this paper [3], can be used to correlate the experimental data. In principle, and within the limits of dimensional similitude, these models could be used to extrapolate the measurements of sealing effectiveness made on the experimental rig at one set of operating conditions to an engine operating at another set of conditions.

Part 2 of this paper describes an experimental investigation of ingress where there is no main-stream flow, and consequently no circumferential variation of external pressure, in the annulus. Owen [1, 2] described this axisymmetric type of ingestion as *rotationally-induced* (RI) ingress. Unlike EI ingress, where the pressure differences in the main gas path govern ingestion, RI ingress occurs when the effects of rotation in the wheel-space are important. In gas turbines, EI ingress is usually the controlling mechanism for ingestion. However, in double rim seals (like that shown in Fig. 1) the circumferential variation in pressure is attenuated in the annular space between the two seals. If the annular space is large enough to damp out the pressure asymmetry, EI ingress can dominate for the outer seal and RI ingress can dominate for the inner one.

2. BRIEF REVIEW OF PREVIOUS WORK

As ingress has been extensively reviewed by Owen *et al.* [1-5], only a brief review of the papers that are relevant to EI ingress is included here. RI ingress is reviewed in Part 2 of this paper. Symbols are defined in the nomenclature.

2.1 EI ingress

Abe *et al.* [6], who used a turbine rig with vanes in the annulus upstream of the rim seal but with no downstream blades, were the first to show that ingress could be governed by the external flow in the annulus rather than by the rotational speed of the disc. The authors tested several rim-seal geometries and identified ingress as predominantly governed by the following: the ratio of the velocities of the sealing air and the flow in the annulus; the rim-seal clearance; and the shape of the rim-seal.

Phadke and Owen [7-9] conducted experiments in a rig without vanes or blades and, using blockages in the external annulus, examined the influence of pressure asymmetries on seal performance. For EI ingress, they determined $C_{w,min}$, the non-dimensional sealing flow rate required to prevent ingestion, for different rim-seal geometries. They observed $C_{w,min}$ was (i) independent of Re_{ϕ}, (ii) increased with increasing Re_w, the axial-flow Reynolds number in the external annulus, and (iii) increased linearly with $C_{p,max}^{1/2}$, the non-dimensional pressure difference in the external annulus. Phadke and Owen correlated their results as follows:

$$C_{w,\min} = \pi K G_c \left(2C_{p,\max}\right)^{1/2} \mathrm{Re}_w \tag{2.1}$$

where G_c is the seal-clearance-to-radius ratio ($= s_c / b$) and K is an empirical constant; the data for a variety of seals were correlated with $K = 0.6$.

Hamabe and Ishida [10] and Dadkhah *et al.* [11] made measurements of the sealing effectiveness in a turbine rig fitted with upstream guide vanes but with no downstream blades. Both showed the importance of the annulus pressure asymmetries on ingestion.

The first published data for a turbine rig with both vanes and blades was presented by Green and Turner [12]. Bohn *et al.* [13] made measurements of sealing effectiveness in a rig with a 1.5 stage turbine (stator-rotor-stator). Gentilhomme *et al.* [14] made ingress measurements and carried out computations for a single-stage turbine rig with both vanes and blades. The circumferential pressure in the annulus, obtained by CFD, was used in conjunction with an orifice model to estimate the effectiveness.

The Aachen group conducted many ingress studies in turbine rigs with vanes and blades. Bohn and Wolff [15] presented a correlation for the sealing effectiveness in terms of $C_{w,min}$, G_c and $C_{p,max}$, and their correlations display the linear variation of $C_{w,min}$ with $C_{p,max}^{1/2}$ shown by eq. (2.1). Bohn and Wolff showed that the performance of rim-seals could be ranked using different values of K.

Johnson *et al.* [16] used an orifice model to calculate the effectiveness measurements in the turbine rig of Bohn *et al.* [17]. They used 2D time-dependent CFD for the external circumferential pressure distribution in their model, which allowed the effects of the vanes and blades to be taken into account. A modified version of their orifice model was also successfully applied by Johnson *et al.* [18] to the ingress measurements made on a turbine rig in Arizona State University.

CFD has been used with some success for the ingress problem, but care must be exercised in computing these unsteady 3D flows. The reader is referred to Zhou *et al.* [19] who provide a review of some of the recent CFD papers related to ingress.

2.2 Orifice model for EI ingress

In references [1, 2, 4, 5], orifice models recently developed at the University of Bath have had good success in calculating the sealing effectiveness of rim seals for EI ingress. These models treat the seal clearance as an orifice and use variations of Bernoulli's equation, including swirl terms, to relate the sealing flow rate to the pressure drop across the seal. Although the equations are derived for inviscid incompressible flow, discharge coefficients, analogous to those used for the standard orifice equations, are introduced to account for losses. In general, different discharge coefficients ($C_{d,i}$ and $C_{d,e}$) are needed for ingress and egress, and these have to be determined empirically.

Owen *et al.* [5] show that EI ingress is governed predominantly by the magnitude of the peak-to-trough circumferential difference in pressure; the shape of the pressure distribution is of secondary importance for the calculation of ingress. The orifice model provides a simple equation that expresses ε, the sealing effectiveness, in terms of Φ_o, the non-dimensional sealing flow rate.

The relationship between the model and measured values of ε and Φ_o depends on only two empirical parameters. Further, the model provides the important advantage of providing an estimate of $\Phi_{min,EI}$, the minimum sealing flow rate to prevent ingress, from the (ε, Φ_o) data points without any knowledge of the pressure distribution in the annulus or any associated rim-seal discharge coefficients; this makes the model a powerful tool for rim-seal design.

Only the principal solutions to the orifice equations are given below; for details of their derivation (and the application of the model to RI ingress) the reader is referred to Part 2 of this paper.

The non-dimensional sealing flow parameter is defined as follows:

$$\Phi_o = \frac{C_{w,o}}{2\pi G_c Re_\phi} \tag{2.2}$$

As Re_ϕ and $C_{w,0}$ include viscous terms which cancel in the above equation, this definition disguises the fact that Φ_o is an inertial parameter. It is more appropriate to use an alternative definition, which is equivalent to eq (2.2):

$$\Phi_o = \frac{U}{\Omega b} \tag{2.3}$$

where U is the bulk mean radial velocity of sealing air through the seal clearance, so that

$$U = \frac{\dot{m}_o}{2\pi\rho b s_c} \tag{2.4}$$

The symbols Φ_e, Φ_i and Φ_o denote the flow parameters for egress, ingress and the sealing flow, respectively. Φ_{min} is the value of Φ_o when the system is sealed, so that $C_{w,o} = C_{w,min}$. That is,

$$\Phi_{min} = \frac{U_{min}}{\Omega b} = \frac{C_{w,min}}{2\pi G_c Re_\phi} \tag{2.5}$$

From the continuity equation,

$$\Phi_o = \Phi_e - \Phi_i \tag{2.6}$$

and, for $\Phi_o < \Phi_{min}$, the sealing effectiveness can be calculated from

$$\varepsilon = 1 - \frac{\Phi_i}{\Phi_e} = \frac{\Phi_o}{\Phi_e} = \frac{\Phi_o}{\Phi_o + \Phi_i} \tag{2.7}$$

That is, $\varepsilon = 0$ when $\Phi_o = 0$, and $\varepsilon = 1$ when $\Phi_o = \Phi_{min}$.

Although the effectiveness is a convenient parameter, the designer wants to know how much hot gas enters the wheel-space when $\Phi_o < \Phi_{min}$. This involves calculating Φ_i where, from eq (2.7)

$$\frac{\Phi_i}{\Phi_o} = \varepsilon^{-1} - 1 \tag{2.8}$$

Another parameter that is widely used in the orifice equations is Γ_c, the ratio of the discharge coefficients, which is defined by

$$\Gamma_c = \frac{C_{d,i}}{C_{d,e}} \tag{2.9}$$

It should be noted that $C_{d,e}$ and $C_{d,i}$ are empirical constants.

For EI ingress, ΔC_p, the non-dimensional pressure difference, is the driving force for ingress. This is defined as

$$\Delta C_p = \frac{\Delta p}{1/2\, \rho\, \Omega^2\, b^2} \tag{2.10}$$

where Δp is the time-average peak-to-trough difference in static pressure in the annulus.

2.3 Effectiveness equation for EI ingress

In [2], a linear 'saw-tooth model' was used to approximate the time-average circumferential distribution of pressure in the external annulus. Owen *et al.* [5] showed that the saw-tooth model performed equally well to curves more closely fitted to the pressure distribution. The saw-tooth model allows the orifice equations to be solved analytically, so that

$$\Phi_{min,EI} = 2/3\, C_{d,e} \Delta C_p^{\,1/2} \tag{2.11}$$

It is useful to express the constant K in eq. (2.1), which was used by Phadke and Owen [7-9] and by Bohn and Wolff [15], in terms of $\Phi_{min,EI}$ and ΔC_p:

$$\Phi_{min,EI} = \frac{C_{w,min,EI}}{2\pi G_c\, Re_\phi} = K\sqrt{\frac{\Delta C_p}{2}} \tag{2.12}$$

Implicit equations for EI effectiveness were derived in [2] but more convenient explicit equations are obtained in Part 2 of this paper [3], where for $\Phi_o < \Phi_{min,EI}$:

$$\frac{\Phi_o}{\Phi_{min,EI}} = \frac{\varepsilon}{[1+\Gamma_c^{-2/3}(1-\varepsilon)^{2/3}]^{3/2}} \tag{2.13}$$

For $\Phi_o > \Phi_{min,EI}$, $\varepsilon = 1$, and eq (2.12) is referred to as the *EI effectiveness equation.*

It should be noted that the two empirical constants, $C_{d,e}$ and $C_{d,i,}$ in the orifice equations are replaced by two unknown parameters, $\Phi_{min,EI}$ and $\Gamma_{c,}$ in eq (2.13). Zhou *et al.* [20] describe how the effectiveness equations for both EI and RI ingress can be fitted to experimental data using a statistical model to find the best estimates of these parameters, and this is discussed in Part 2 [3].

For the designer, $\Phi_{min,EI}$ (which determines how much sealing air is required to prevent ingress) is more important than Γ_c. However, the value of Γ_c affects the shape of the effectiveness curve (i.e. the variation of ε with $\Phi_o / \Phi_{min,EI}$), and for a given value of Φ_o the effectiveness decreases as Γ_c increases.

It follows from eqs (2.7) and (2.13) that

$$\frac{\Phi_{i,EI}}{\Phi_{min,EI}} = \frac{1-\varepsilon}{[1+\Gamma_c^{-2/3}(1-\varepsilon)^{2/3}]^{3/2}} \tag{2.14}$$

In the limit that $\Phi_o = 0$, where $\varepsilon = 0$, eq (2.14) reduces to

$$\frac{\Phi_{i,EI}\,^*}{\Phi_{min,EI}} = \frac{1}{[1+\Gamma_c^{-2/3}]^{3/2}} \tag{2.15}$$

where $\Phi_{i,EI}$* denotes that $\Phi_o = 0$; this is the maximum value of the non-dimensional ingested flow rate that can enter the wheel-space. For $\Gamma_c = 1$, $\Phi_{i,EI}^* / \Phi_{min,EI} = 0.35$; that is, for this case the maximum flow that can be ingested is 35% of the flow required to seal the system.

2.4 Some comments on the effectiveness equation

It can be seen from eqs (2.13) and (2.14) that the variation of ε or $\Phi_{i,EI}$ with Φ_o depends only on the two parameters $\Phi_{min,EI}$ and Γ_c. This means that the EI effectiveness equation has uncoupled ingress from its driving force, ΔC_p – cause has been separated from effect.

As explained in [5], there are conditions for mathematical consistency between eqs (2.11) and (2.13). The consistency criterion shows that the locations in the annulus where ΔC_p should be determined are very restricted, and the criterion is unlikely to be satisfied by experimental measurements of ΔC_p. Consequently, the value of $C_{d,e}$ determined from eq (2.11), or the value of K from eq. (2.12), will depend on where in the annulus ΔC_p is measured; this means that $C_{d,e}$ and K are of limited practical importance. However, the value of ΔC_p (wherever it is measured) is necessary for extrapolating the effectiveness measurements from rig to engine; this is discussed further in Section 5.

3. EXPERIMENTAL FACILITY

This section describes a new research facility which experimentally models hot gas ingestion into the wheel-space of an axial turbine stage. Measurements of CO_2 gas concentration in the rim seal region inside the wheel-space were used to determine the variation of ε_c with Φ_o for two generic (though engine-representative) rim-seal geometries. The distribution of ε_c with radius is presented in Part 2.

3.1 Test rig

The test section of the facility, shown in Fig. 4a, features a turbine stage with 32 vanes and 41 blades which were formed from nylon by rapid-prototyping. The disc to which the blades were attached could be rotated up to 4000 rpm by an electric motor, and the blades were symmetric NACA 0018 aerofoils to avoid the necessity of a dynamometer to remove the unwanted power.

Compressed air entered the mainstream annulus of the stage through a convergent transition section fed from 32 circular pipes, each of 25.4 mm diameter, some of which are shown in Fig. 4b.The upstream end of each pipe was connected to a radial diffuser (not shown in the figure) where the delivery pressure to each pipe was measured to be equal within ± 5%. Air exhausted from the stage to the atmosphere. All flow rates to the test section were measured using calibrated orifice plates (built to EN ISO 5167-2).

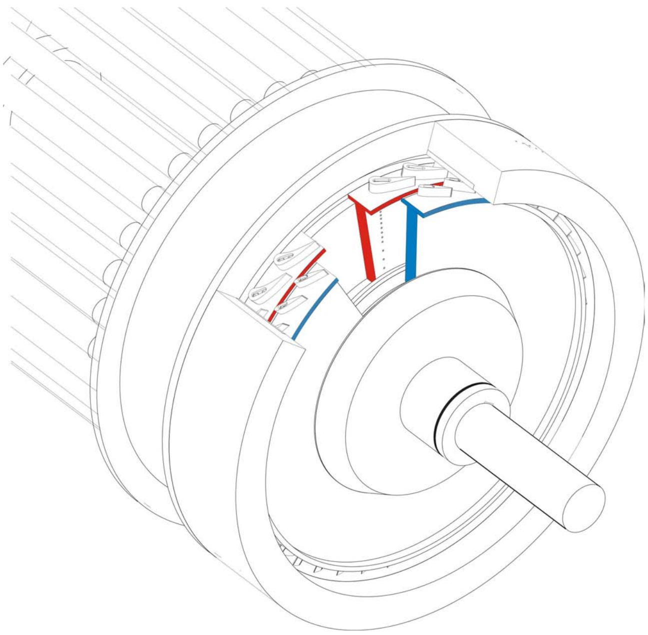

Fig. 4a: Rig test section showing turbine stage

The vanes and blades were secured to aluminium platforms which form the periphery of the stator and rotor respectively. Both the stationary and rotating discs (highlighted in red and blue, respectively, in Figs. 4a/b) were manufactured from transparent polycarbonate to allow optical access to the wheel-space for the future application of thermochromic liquid crystal to heat transfer measurements.

The disc could be rotated up to speeds of 4000 rpm, providing a maximum rotational Reynolds numbers, Re_ϕ (based on disc radius) up to 1.1 x 10^6. This value is typically an order-of-magnitude less than those found in gas turbines. However, Owen and Rogers [21] have shown that, for rotating flow, the turbulent flow structure in the boundary layers is principally governed by the turbulent flow parameter, λ_T, and depends only weakly on Re_ϕ. Hence the flow structure in the rig is considered to be representative of that found in the cooling systems of engines.

Sealing air was introduced into the wheel-space at a low radius through an inner seal. To measure the degree of ingestion, this sealing flow was seeded with a carbon dioxide tracer gas. The concentration of CO_2 was monitored at the entrance to the wheel-space, c_0, and in the unseeded upstream flow through the annulus, c_a. The variation of concentration c_s with radius ($0.55 < r/b < 0.993$) along the stator disc in the wheel-space was determined by sampling through 15 tubes of diameter 1.6 mm. These tubes (or taps) are illustrated in Fig. 4a and gas is drawn by a pump which led the samples to an infra-red gas analyser.

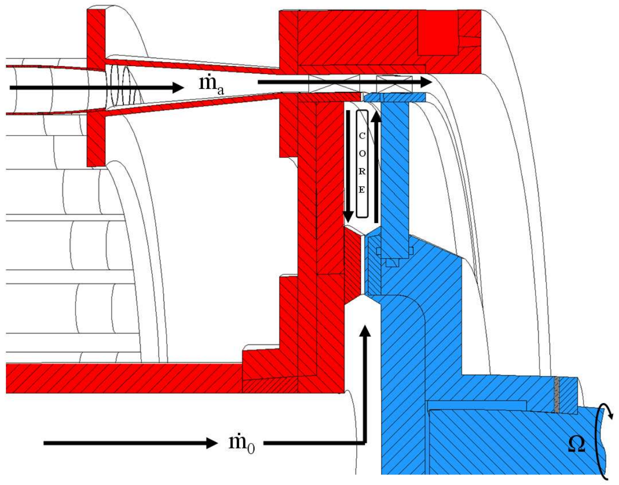

Fig. 4b: Rig test section showing sealing and mainstream flows (red, stationary; blue, rotating)

The following definition of gas-concentration effectiveness, ε_c is used:

$$\varepsilon_c = \frac{c_s - c_a}{c_o - c_a} \qquad (3.1)$$

where the subscripts a, o and s refer respectively to the air in the annulus, the sealing air at inlet to the system and the stator surface. From eq (2.8) for the ingress parameter, it follows that

$$\frac{\Phi_{i,EI}}{\Phi_o} = \frac{c_o - c_s}{c_s - c_a} \qquad (3.2)$$

It follows that $\varepsilon_c = 1$ when there is no ingress and $\varepsilon_c = 0$ when the sealing flow rate is zero. As discussed above with reference to Fig. 3, the value of ε_c is expected to be relatively insensitive to the radial location on the stator. This is shown to be the case in Part 2, and the rim-seal effectiveness reported here is based on data collected at $r/b = 0.958$. The measurements of effectiveness are time averaged and the completion of a full radial traverse of concentration took approximately 20 minutes.

Concentration measurements were made using a Signal Group 9000MGA multi-gas analyzer, applying an infra-red filter-correlation technique to calculate seed-gas concentration level. The concentration measurements were made within a combined uncertainty of +/- 1.5% of the measured value. The analyzer was calibrated using an alpha-grade pure N_2 as zero-gas and a 3% CO_2 in N_2 as the span-gas; acting as start and end points for the linear calibration, respectively. The sealant gas flow-rate in which the CO_2 seed is injected was measured to within +/- 3% uncertainty using the aforementioned orifice plate.

The effectiveness, ε, used in the orifice model defined by eq (2.7) is based on the convection of fluid created by pressure differences. In the mass-transfer equation, concentration differences in the fluid create diffusion and mixing, which are additional to the convection of fluid calculated by the orifice model. Consequently, the two definitions of effectiveness are similar but are not generally equivalent. Despite this, it is usual to match the measured and theoretical results by implicitly assuming that they are equivalent.

In addition to the concentration taps, static pressure taps (diameter 0.5 mm) were located at 15 radial stations in the stator, and seven pitot-tubes enabled the measurement of the radial distribution of static and total pressure, and of V_ϕ, the tangential velocity of the air in the core outside the boundary layers.

Two different rim seals were investigated: these are shown in Fig. 5 and geometric details (static and under rotation) are given in Table 1. The vane and blade platforms at the periphery of the parallel stator and rotor discs form a simple axial-clearance seal (Fig. 5a). The generic radial-clearance seal shown in Fig. 5b features an identical geometry at the periphery of the stationary disc, with an axial overlap from a seal lip positioned at a lower radius on the rotating disc. The radial-clearance seal bolts into the rotor under the platform and a modular design allows a range of generic and company-proprietary seals to be tested.

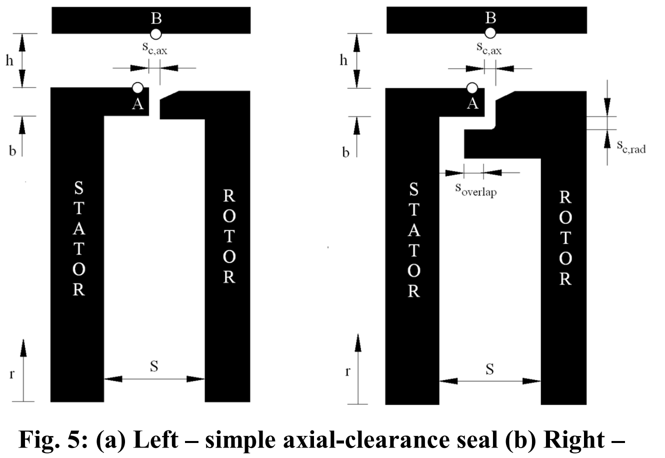

Fig. 5: (a) Left – simple axial-clearance seal (b) Right – generic radial-clearance seal

Displacement transducers were used to measure the axial deflection of the disc. The axial clearance of the seal was found to increase slightly when under rotation and when sealing flow pressurised the wheel-space, but at the maximum value of Φ_o = 0.38 tested the variation in $s_{c,ax}$ was < 8% of the clearance. Displacement transducers were also used to measure the radial growth of the disc, rotor platform and radial-clearance seal under rotation, from which the operating seal clearances were determined.

Geometric Symbol	Axial-Clearance Seal	Radial-Clearance Seal
h	10 mm	
b	190 mm	
S	20 mm	
$s_{c,ax}$	2 mm	
$G_{c,ax}$	0.0105	
$s_{overlap}$	-	3.7 mm
$s_{c,rad,0}$ (0 rpm)	-	2.400 mm
$G_{c,rad,0}$ (0 rpm)	-	0.0126
$G_{c,rad}$ (2000 rpm)	-	0.0124
$G_{c,rad}$ (3000 rpm)	-	0.0121
$G_{c,rad}$ (3500 rpm)	-	0.0119

Table 1: Geometric properties for both seal configurations

Fig. 6 shows the variation of $\delta = s_{c,rad} - s_{c,rad,0}$ and $\delta / s_{c,rad,0}$ with $\Omega^2 b^2$. Here $s_{c,rad,0}$ is the radial clearance at zero rotation and Ωb is the rotational speed of the disc. The radial clearance is seen to decrease linearly with the square of the disc speed, with $\delta / s_{c,rad,0}$ < 6% at the maximum speed tested, and the value of $G_{c,rad}$ varied by approximately 4% as the disc speed increased from 2000-3500 RPM (see Table 1). Also shown in the figure are finite element analysis (FEA) calculations which agree well with the measurements.

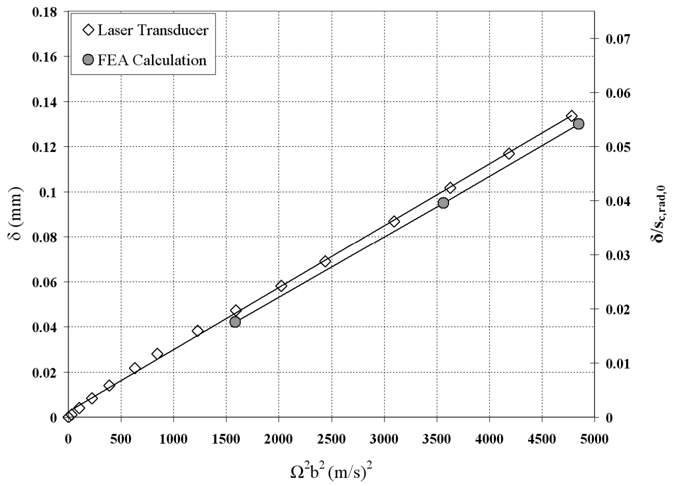

Fig. 6: Radial displacement of radial-clearance seal measured at the seal-tip

The vanes and blades in the annulus produced a flow structure representative of those found in engines, albeit at lower Reynolds and Mach numbers. Fig. 7 shows the geometry of the generic vanes and blades; the latter being a symmetric NACA 0018 aerofoil. The axial distance between the vane trailing edge and the blade leading edge was 12 mm (or 0.52 vane axial chords). The centre line of the 2 mm seal gap was equidistant between the vane and blade.

The circumferential variation of static pressure was determined from 15 taps (each 0.5 mm diameter) arranged across one vane pitch, as illustrated in Fig. 7; these taps were located in the vane platform 2.5 mm downstream of the vane trailing edge (location A) and in the outer casing above the centre-line of the seal clearance (location B), as marked in Fig. 5. Data was averaged over four vane pitches.

Fig. 7 also shows the velocity triangles for the turbine stage. The air leaves the vane at angle α with velocity C and corresponding Mach number $M = C/a$. The axial component of velocity is W, with corresponding axial Reynolds number $Re_W = \rho Wb/\mu$.

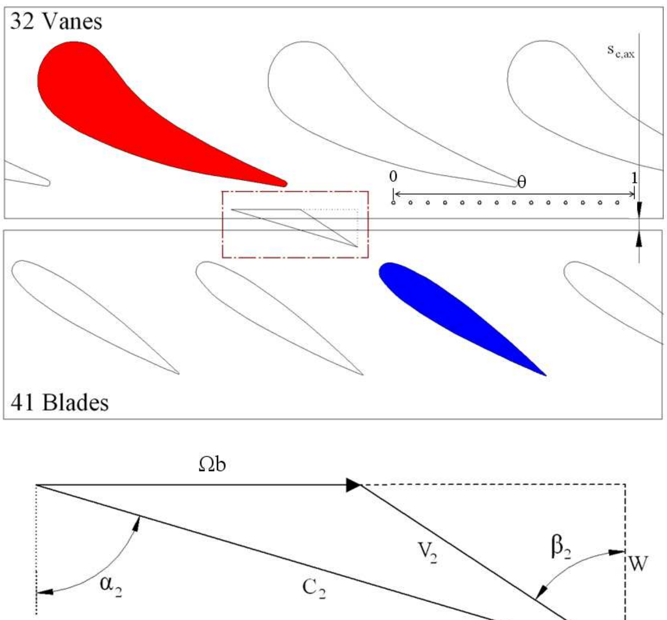

Fig. 7: Generic vane and blade geometry and associated velocity triangles

The flow exiting the vanes is virtually incompressible and near atmospheric pressure; the density, ρ, speed of sound, a, and air viscosity, μ, are determined from the static temperature and pressure measured inside the wheel-space on the stator at r/b = 0.993. The rotor inlet angle and velocity are β and V. At the *design condition*, $\beta = \beta_0$ though the rig (or engine) can be operated off design: $\beta - \beta_0 > 0$ is referred to as the under-speed case and $\beta - \beta_0 < 0$ the over-speed case. For the rig, $\beta_0 = 56^o$, $\alpha = 73^o$, and $Re_W / Re_\phi = 0.538$. All rim-seal effectiveness data presented in this paper are for the design condition, with similar velocity triangles at the three *operating points* listed in Table 2.

Parameter	Disc Speed (RPM)		
	2000	3000	3500
Re_Φ	5.32 x 10^5	8.17 x 10^5	9.68 x 10^5
Re_w	2.86 x 10^5	4.40 x 10^5	5.21 x 10^5
Re_w/Re_Φ	0.538	0.538	0.538
M	0.225	0.339	0.398

Table 2: Design operation points for experimental facility

3.2 Circumferential variation of pressure in the annulus

The time-average static pressure, p_2, in the annulus and the peak-to-trough pressure difference, Δp, are proportional to W^2, where W is the axial component of velocity in the annulus. From the definitions given in the Nomenclature, it follows that the pressure coefficient, C_p, and the non-dimensional pressure difference, ΔC_p, are therefore proportional to $(Re_w/Re_\phi)^2$. As shown in Table 2, (Re_w/ Re_ϕ) = 0.538 at the design point.

The circumferential distribution of C_p is shown in Fig. 8a at locations A (vane platform) and B (on the outer casing at the axial location of the middle of the seal clearance). The measurements were made at the design point for the case of no sealing flow, *i.e.* $\Phi_o = 0$, and the results at location A are shown for three values of Re_ϕ. It should be noted that the flow is over a small range of Mach numbers.

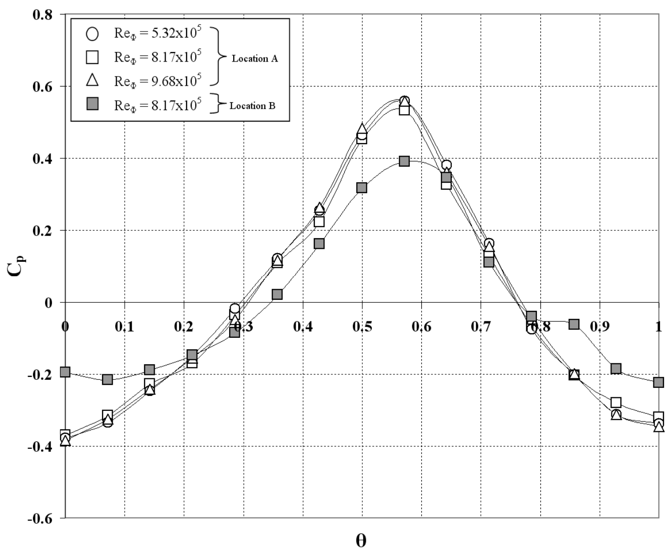

Fig. 8a: Effect of Re_Φ on circumferential distribution of C_p over non-dimensional vane pitch. (Re_w/Re_ϕ) = 0.538

It can be seen in Fig. 8a that, as Re_w/Re_ϕ is constant, the three distributions at location A are virtually independent of Re_ϕ. However, they differ significantly from the distribution at location B, and the non-dimensional peak-to-trough pressure difference, ΔC_p, at A is greater than that at B. Swirl causes a radial pressure gradient so that the pressure will increase in the radial direction, whereas the pressure is expected to decrease with axial distance from the vane; the axial decrease evidently dominates causing the observed reduction at location B. *It should be noted that ΔC_p depends on where it is measured.*

Fig. 8b illustrates the measured circumferential distribution of C_p for Re_ϕ = 8.17x10^5 at the design point at location A for three different values of Φ_0 / $\Phi_{min,EI}$. The peak-to-trough pressure difference decreases slightly as Φ_0 increases. This decrease, which is attributed to the 'spoiling effect' of the egress as it interacts with the main flow in the annulus, is consistent with findings of Bohn *et al.* [13]. In the results presented below, ΔC_p is given for Φ_0 = 0, which is the case used by most experimentalists.

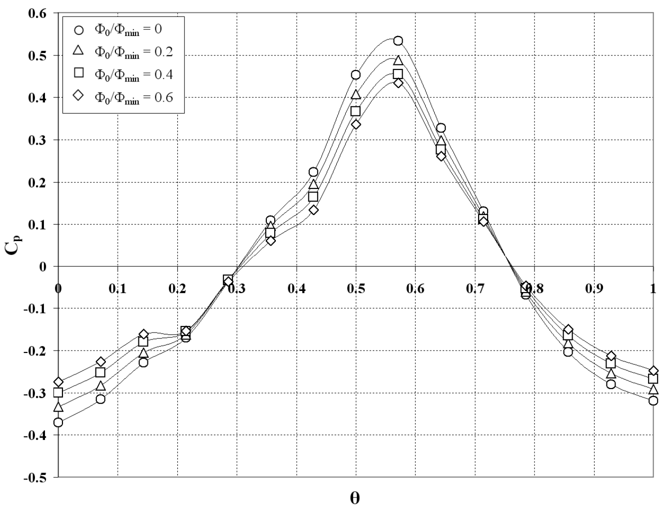

Fig. 8b: Effect of Φ_0 / $\Phi_{min,EI}$ on circumferential distribution of C_p over non-dimensional vane pitch. Re_ϕ = 8.17x10^5 (Re_w/Re_ϕ) = 0.538

Fig. 8c shows the expected linear variation of $\Delta C_p^{1/2}$ with Re_W / Re_ϕ at the two locations (A and B) in the annulus. The data was collected for Re_ϕ = 5.32x10^5 and 8.17x10^5 over the range 0 < Re_W < 4.9x10^5. For the given vane and blade geometry, the ratio Re_W / Re_ϕ uniquely determines the stage velocity triangles and, as stated above, ΔC_p. The angle $\beta - \beta_0$ is plotted on the upper axis and at the design condition, $\beta - \beta_0$ = 0 and Re_W / Re_ϕ = 0.538. As $|\beta - \beta_0|$ increases, the rig operates further from the design point and $\Delta C_p^{1/2}$ increases and decreases linearly with Re_W / Re_ϕ for $\beta - \beta_0 > 0$ and $\beta - \beta_0 < 0$ respectively. In this paper only the design point has been used for rim-seal effectiveness measurements.

The above results clearly illustrate that (for a given rim seal and turbine-stage geometry) the value of $C_{d,e}$ determined from eq (2.11), or the value of K from eq (2.12), will depend on where in the annulus ΔC_p is measured. It is therefore difficult to compare the values of $C_{d,e}$ and K obtained in one set of experiments or computations with another. Fortunately, these 'secondary parameters' are unnecessary in the determination of $\Phi_{min,EI}$, which is the principal empirical characteristic of the rim seal for a prescribed set of velocity triangles and fluid-dynamic conditions and in the annulus.

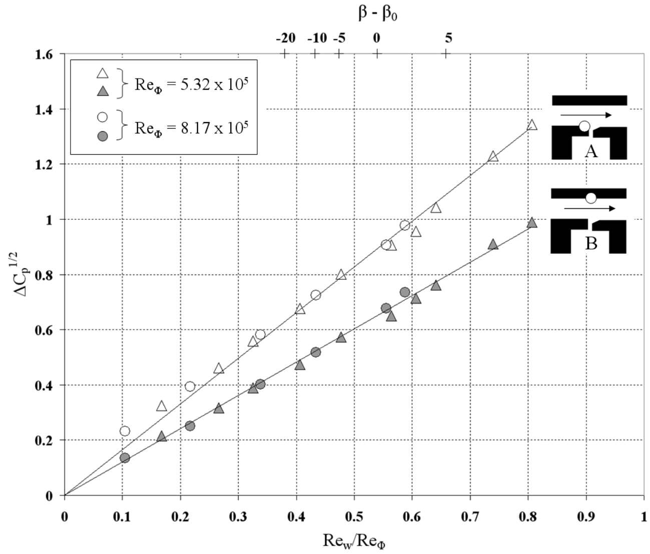

Fig. 8c: Effect of Re_ϕ on variation of $\Delta C_p^{1/2}$ with Re_W / Re_ϕ at locations A and B in annulus

4. MEASUREMENTS OF RIM-SEAL EFFECTIVENESS

In this section, experimental data collected using the generic axial- and radial-clearance seals shown in Fig. 5 are presented. The rim-seal effectiveness is measured using the concentration effectiveness, ε_c , which is defined by eq. (3.1), collected on the stator at r/b = 0.958. (The distribution of ε_c in the wheel-space, which is presented in Part 2, was found to be relatively insensitive to the radial location on the stator.) Data is presented in terms of $C_{w,o}$, the widely used non-dimensional sealing flow rate, as well as Φ_0 , the non-dimensional flow parameter used in the orifice equations. The experimental data is compared with theoretical calculations from the orifice model using the effectiveness equations, eqs. (2.13) and (2.14).

4.1 Rim-seal effectiveness in terms of $C_{w,o}$

Figure 9a shows the variation of effectiveness with $C_{w,o}$, for the two rim seals. Measurements were made at three values of Re_ϕ corresponding to the three operational points listed in Table 2 with Re_W / Re_ϕ = 0.538. Thumb-nail sketches of the two seal configurations are shown on this and all following figures, and it should be noted that the external flow is from left to right (*i.e.* from the stator towards the rotor).

The data illustrate that ε_c increases with increasing $C_{w,o}$, as the sealing flow pressurises the wheel-space and reduces ingestion of main-stream flow from the annulus. As Re_ϕ (hence

Re_w) increases, a larger $C_{w,o}$ is required to maintain a given level of effectiveness; $C_{w,min}$, the non-dimensional sealing flow required to seal the wheel-space correspondingly increases with Re_ϕ and Re_w . The radial-clearance seal is shown to require a significantly smaller $C_{w,min}$ than the axial-clearance seal for the same Re_ϕ, demonstrating the former to be a superior geometric design in terms of rim-seal effectiveness.

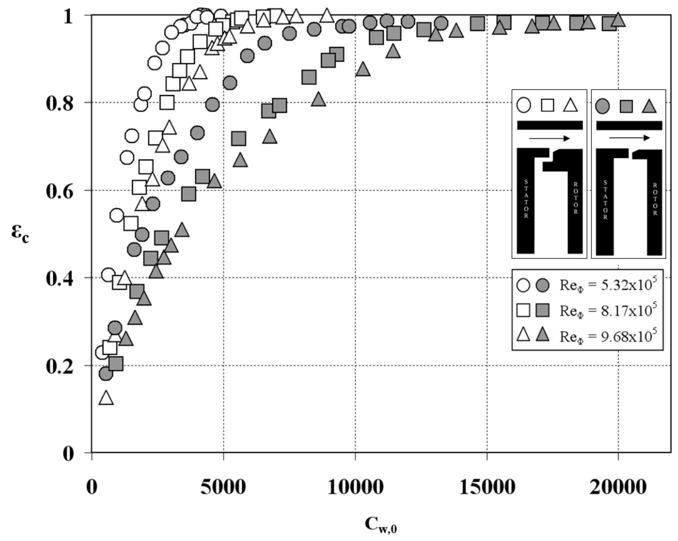

Fig. 9a: Effect of Re_ϕ on measured variation of ε_c with $C_{w,o}$ for both tested rim seals. (Open symbols denote radial-clearance seal; solid symbols denote axial-clearance seal.)

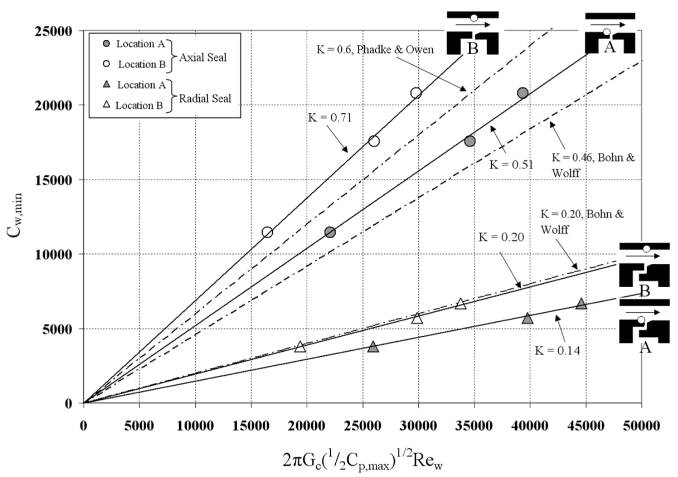

Fig. 9b: Variation of $C_{w,min}$ with $C_{p,max}{}^{½}$ Re_W, highlighting seal comparisons using K

Figure 9b shows the linear variation of $C_{w,min}$ with $C_{p,max}{}^{½}$ Re_W consistent with eq. (2.1), and data presented by Phadke and Owen [7-9] and Bohn and Wolff [14]. Data for both the axial- and radial-clearance seals are shown for $C_{p,max}$ based on the peak-to-trough difference in static pressure obtained at the two measurement positions (A and B) in the annulus.

K, which is defined by eq (2.12), is a parameter commonly used for ranking the relative performance of different rim-seal geometries. The value of K, which is shown in Fig. 9b, depends upon the measurement location of $C_{p,max}$. Phadke and Owen correlated their data with K = 0.6, and Bohn and Wolff correlated their data for a similar axial-clearance seal and a radial-clearance seal with K = 0.46 and 0.20 respectively. In light of the discussion in section 3.2 above, it is surprising and perhaps fortuitous that these values of K are as close as they are to those obtained here!

4.2 Rim-seal effectiveness in terms of Φ_o

The data in Fig. 9a have been re-plotted versus Φ_o in Fig. 10a. Note that the radial-clearance seal has slightly varying values of G_c at different Re_ϕ, as shown in Table 2. Instead of having to use separate correlations for the effects of G_c and Re_ϕ on ε, Φ_o combines $C_{w,o}$, G_c and Re_ϕ into a single flow parameter. For the design condition (for which the ratio Re_w/Re_ϕ = 0.538), the rim seals are shown to be characterised by $\Phi_{min,EI}$, which is independent of Re_ϕ .

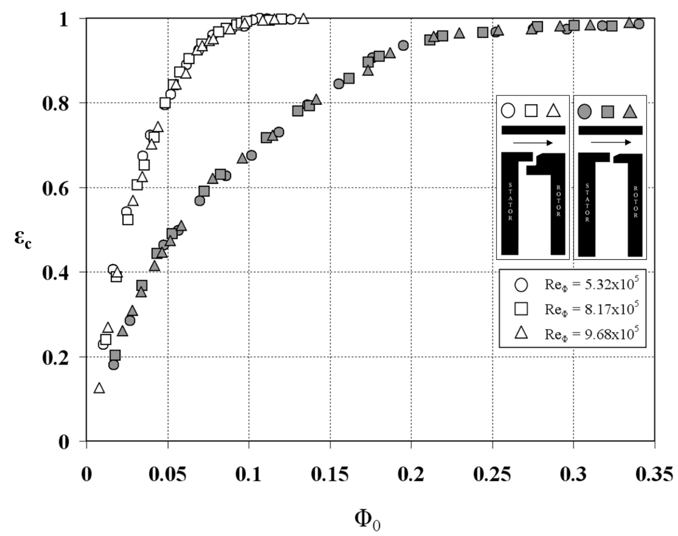

Fig. 10a: Measured variation of sealing effectiveness with Φ_0 for EI ingress for (Re_w/Re_ϕ) = 0.538 (Open symbols denote radial-clearance seal; solid symbols denote axial-clearance seal.)

Eqs (2.13) and (2.14), the effectiveness equations derived from the orifice model, include the two parameters, $\Phi_{min,EI}$ and Γ_c. Fig. 10b shows a comparison between the experimental data and the theoretical variation of effectiveness according to these equations for the axial-clearance seal, and Fig. 10c shows results for the radial-clearance seal. The ingested flow rate, not shown in Fig. 9a, is presented as the non-dimensional parameter $\Phi_{i,EI}$, which was obtained from eq. (3.2).

The fit between these equations and the measured variation of ε_c with Φ_o was optimised, in terms of $\Phi_{min,EI}$ and Γ_c, using a statistical model featuring maximum likelihood estimates described by Zhou *et al.* [19]. Figs 10b and 10c show that the agreement between the optimum theoretical curves and the experimental data is very good

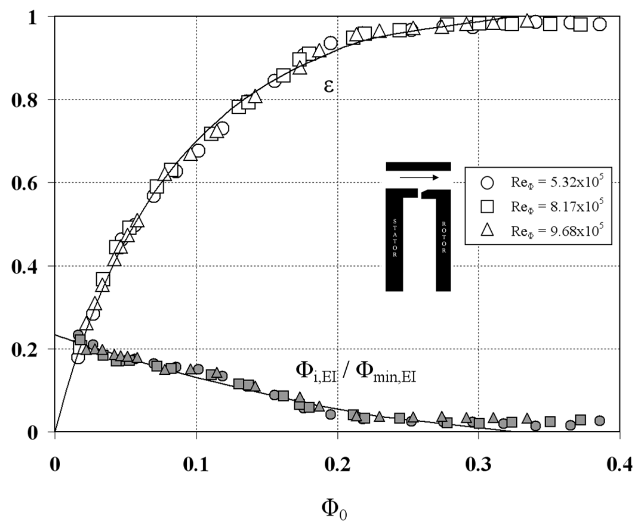

Fig. 10b: Comparison between theoretical effectiveness curves and experimental data for axial-clearance seal with EI ingress for *(Re$_w$/Re$_\phi$)* = 0.538 (Open symbols denote ε data; closed symbols denote $\Phi_{i,EI}$ /$\Phi_{min,EI}$ data; solid lines are theoretical curves.)

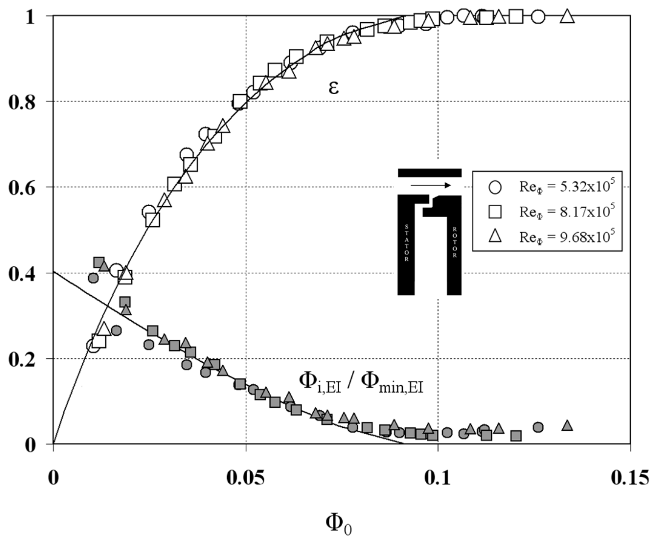

Fig. 10c: Comparison between theoretical effectiveness curves and experimental data for radial-clearance seal with EI ingress for *(Re$_w$/Re$_\phi$)* = 0.538 (Open symbols denote ε data; closed symbols denote $\Phi_{i,EI}$ /$\Phi_{min,EI}$ data; solid lines are theoretical curves.)

The values of $\Phi_{min,EI}$ and Γ_c,, as well as the standard deviation σ between the equation and the data , for the two seals are shown in Table 3. The table includes the values of $\Phi_{i,EI}$* calculated from eq (2.15). $\Phi_{i,EI}$*is the maximum value of $\Phi_{i,EI}$, which occurs when $\Phi_o=0$; this theoretical value cannot be easily determined from the concentration measurements. Zhou *et al.* recommended that at least 16 data points are needed to produce accurate estimates, and the values of n shown in Table 3 are well in excess of this number.

Seal	Axial clearance	Radial clearance
$\hat{\Phi}_{min}$	0.326	0.0915
$\hat{\Phi}_{min}^{-}$	0.309	0.0869
$\hat{\Phi}_{min}^{+}$	0.344	0.0962
$\Phi_{i,EI}$*	0.0764	0.0371
$\hat{\Gamma}_c$	0.476	1.32
$\hat{\Gamma}_c^{-}$	0.421	1.09
$\hat{\Gamma}_c^{+}$	0.545	1.63
n	60	54
σ	0.0146	0.0184

Table 3: Parameters for axial-clearance and radial-clearance seals, determined using method of Zhou *et al.* [19] for the *n* data points. (^ denotes estimated value from the theory, and + - denote upper and lower bounds of 95% confidence intervals.)

Table 3 also shows that, for EI ingress, the ratio of Φ_{min} for the radial-clearance seal to that required for the axial-clearance seal is around 26%. The radial-clearance seal is significantly more effective that the axial-clearance seal. This result is consistent with the experiments of Bohn and Wolff [14].

4.3 Rim-seal discharge coefficients

Table 4 shows the values of $C_{d,e}$, $C_{d,i}$ and K for the two seals. The $C_{d,e}$ were calculated from eq (2.11) and the values of $C_{d,i}$ were found from the corresponding value of Γ_c; K was calculated from eq (2.12). For each seal, the values of these three constants depends on where (location A or B) in the annulus ΔC_p was determined. Regardless of location, the value of $C_{d,e}$ for the radial-clearance seal is approximately 28% of that for the axial-clearance seal; the corresponding ratio for the $C_{d,i}$ values is approximately 78%.

The reduction in the amount of sealing air required to prevent ingestion for the radial-clearance seal is a direct consequence of the small value of $C_{d,e}$ for this seal, caused perhaps by the 'impinging jet phenomenon' [21]. (This phenomenon occurs for overlapping radial-clearance seals in which the rotating disc creates an unstable radial wall jet that impinges on the stationary part of the seal.) If this is the case then this phenomenon causes a much larger reduction of $C_{d,e}$ than it does of $C_{d,i}$.

Seal	ΔC_p	Φ_{min}	Γ_c	$C_{d,e}$	$C_{d,i}$	K
Axial 'A'	0.82	0.326	0.48	0.54	0.26	0.51
Radial 'A'	0.82	0.092	1.32	0.15	0.20	0.14
Axial 'B'	0.42	0.326	0.48	0.75	0.36	0.71
Radial 'B'	0.42	0.092	1.32	0.21	0.28	0.20

Table 4: Discharge coefficients and *K* values for both seal configurations

5. PRACTICAL IMPLICATIONS

The object of this section is to suggest how the engine designer might use the experimental results presented here in conjunction with the orifice model. The model has been successful in explaining and calculating the important ingress mechanisms for EI ingress. The question arises: how could the designer estimate the sealing effectiveness in an engine?

As demonstrated here, concentration measurements made on an experimental rig can be used to determine $\Phi_{min,EI}$ and Γ_c for a particular value of ΔC_p . In principle, and within the limits of dimensional similitude, these values should apply to a geometrically-similar engine at the same operating conditions. It is often the case that, even if the geometric conditions are satisfied, the operating conditions (particularly Re_ϕ and M) for the engine will differ from those for the rig. Eq (2.11) shows that, for EI ingress, $\Phi_{min,EI}$ is proportional to $\Delta C_p^{1/2}$, and it is tentatively suggested that this relationship could be used to extrapolate the results from a rig to an engine. Rigs operating under quasi-incompressible fluid-dynamic conditions, as was the case here, may require compressibility corrections for ΔC_p..

Assuming that Γ_c is the same for rig and engine, eqs (2.13) and (2.14) could then be used for design purposes. The new rig at the University of Bath has been specifically designed to test this hypothesis. Future tests will determine the effect of ingress on the temperatures of the rotating and stationary surfaces in the wheel-space. The acid test will be to see if these rig-based results can be applied to an engine.

One final caveat relates to the importance of RI ingress, the subject of Part 2. Unlike EI ingress, where the pressure differences in the main gas path are dominant, RI ingress occurs when the effects of rotation in the wheel-space are dominant. Combined ingress (CI) occurs where the effects of both rotational speed and external flow are significant. If data obtained from an experimental rig is to be extrapolated to an engine then it is important to know that they are both operating in the same part of the CI domain. It has been shown [5] that EI ingress cannot be assumed to occur unless $\Phi_{min,CI} / \Phi_{min,RI} > 2$, and consequently some previous experiments that were thought to have been in the EI regime may well have been in the CI regime.

6. CONCLUSIONS

This paper has described a new research facility which experimentally models gas ingestion into the wheel-space of an axial turbine stage. Measurements of CO_2 gas concentration in the rim-seal region inside the cavity were used to assess the performance of two generic (though engine-representative) rim-seal geometries in terms of the concentration effectiveness, ε_c. Instead of having to use separate correlations for the effects of G_c and Re_ϕ on ε_c, Φ_o (the sealing parameter) combines $C_{w,o}$, G_c and Re_ϕ into a single parameter, and the variation for ε_c and $\Phi_{i,EI}$ is presented against Φ_o . It should also be noted that the flow, which was over a small range of Mach numbers, was virtually incompressible (M< 0.4).

The circumferential variation of the non-dimensional peak-to-trough pressure difference, ΔC_p, in the turbine annulus, which governs this externally-induced (EI) ingestion, was obtained from steady pressure measurements downstream of the vanes and near the rim seal upstream of the rotating blades. At the design point (Re_w/Re_ϕ = 0.538), and at a fixed location in the annulus, ΔC_p, is independent of Re_ϕ. At off-design conditions, $\Delta C_p \propto (Re_w/Re_\phi)^2$.

An orifice model is used to provide simple effectiveness equations, eqs (2.13) and (2.14), that express the variation of ε and $\Phi_{i,EI}$. with Φ_o. The effectiveness equations are able to estimate $\Phi_{min,EI}$, the minimum non-dimensional sealing flow rate to prevent ingress, from the (ε, Φ_o) data points without any knowledge of the pressure distribution in the annulus or any associated rim-seal discharge coefficients; this makes the model a powerful tool for rim-seal design.

The ingestion through the rim seal is a consequence of an unsteady, three-dimensional flow field; the cause-effect relationship between pressure and effectiveness is complex and it may not be possible for an experiment to isolate the many intertwined mechanisms which govern ingress. Despite this, the steady-state experimental data presented here is shown to be successfully correlated by the simple effectiveness equations developed from the orifice model. The data (and model) illustrate that for similar turbine-stage velocity triangles, a rim seal geometry can be characterised principally by the parameter $\Phi_{min,EI}$ which, at the design point, is independent of Re_ϕ .

A statistical model featuring maximum-likelihood estimates was used to fit the effectiveness equations to the experimental data for the two seals. In both cases, the agreement between the fitted curves and the data was very good. Using the statistical model, the ratio of the sealing flow rate required to prevent ingress for the radial-clearance seal to that required for the axial-clearance seal was found to be around 26%.

In principle, and within the limits of dimensional similitude, $\Phi_{min,EI}$ should apply to a geometrically-similar engine operating at the same fluid-dynamic conditions. The orifice model shows that, for EI ingress, $\Phi_{min,EI}$ is proportional to $\Delta C_p^{1/2}$, and it is tentatively suggested that this relationship could be used to extrapolate the results from an experimental rig to an engine.

ACKNOWLEDGEMENTS

This research was funded by EPSRC grant EP/G069107/1. The authors also wish to thank the China Scholarship Council and Beihang University, Beijing, China, for supporting Kunyuan Zhou during his stay at the University of Bath. The research described here is part of a programme jointly funded by the UK Engineering and Physical Sciences Research Council, Siemens Fossil Power Generation and Siemens Oil & Gas.

REFERENCES

[1] Owen, J.M., 2011, “Prediction of Ingestion Through Turbine Rim Seals---Part I: Rotationally Induced Ingress”; ASME J. Turbomach., Vol. 133, Issue 3, 031005-1 to 9.

[2] Owen, J.M., 2011, “Prediction of Ingestion Through Turbine Rim Seals---Part II: Externally Induced and Combined Ingress”; ASME J. Turbomach., Vol. 133, Issue 3, 031006-1 to 9.

[3] Sangan, C. M., Pountney, O. J., Zhou, K., Wilson, M., Owen, J. M., and Lock, G. D., 2011, "Experimental Measurements of Ingestion through Turbine Rim Seals. Part 2: Rotationally-Induced Ingress," ASME Paper GT2011-45313.

[4] Owen, J. M., Pountney, O. J., and Lock, G. D., 2010, "Prediction of Ingress Through Turbine Rim Seals. Part 2: Combined Ingress," ASME Paper GT2010-23349. To appear in ASME J. Turbomach.

[5] Owen, J. M., Pountney, O. J., Zhou, K., Wilson, M., and Lock, G. D., 2010, "Prediction of Ingress Through Turbine Rim Seals. Part 1: Externally-Induced Ingress," ASME Paper GT2010-23346. To appear in ASME J. Turbomach.

[6] Abe, T., Kikuchi, J., and Takeuchi, H., 1979, "An Investigation of Turbine Disk Cooling (Experimental Investigation and Observation of Hot Gas Flow into a Wheel Space)," ASME Paper GT30.

[7] Phadke, U. P., and Owen, J. M., 1988, "Aerodynamic Aspects of the Sealing of Gas-Turbine Rotor-Stator Systems : Part 1: The Behavior of Simple Shrouded Rotating-Disk Systems in a Quiescent Environment," Int. J. Heat Fluid Flow, 9(2), pp. 98-105.

[8] Phadke, U. P., and Owen, J. M., 1988, "Aerodynamic Aspects of the Sealing of Gas-Turbine Rotor-Stator Systems : Part 2: The Performance of Simple Seals in a Quasi-Axisymmetric External Flow," Int. J. Heat Fluid Flow, 9(2), pp. 106-112.

[9] Phadke, U. P., and Owen, J. M., 1988, "Aerodynamic Aspects of the Sealing of Gas-Turbine Rotor-Stator Systems : Part 3: The Effect of Nonaxisymmetric External Flow on Seal Performance," Int. J. Heat Fluid Flow, 9(2), pp. 113-117.

[10] Hamabe, K., and Ishida, K., 1992, "Rim Seal Experiments and Analysis of a Rotor-Stator System with Nonaxisymmetric Main Flow," ASME Paper 92-GT-160.

[11] Dadkhah, S., Turner, A. B., and Chew, J. W., 1992, "Performance of Radial Clearance Rim Seals in Upstream and Downstream Rotor--Stator Wheelspaces," ASME J. Turbomach, 114(2), pp. 439-445.

[12] Green, T., and Turner, A. B., 1994, "Ingestion Into the Upstream Wheelspace of an Axial Turbine Stage," ASME J. Turbomach, 116(2), pp. 327-332.

[13] Bohn, D. E., Decker, A., Ohlendorf, N., and Jakoby, R., 2006, "Influence of an Axial and Radial Rim Seal Geometry on Hot Gas Ingestion Into the Upstream Cavity of a 1.5-Stage Turbine," ASME Paper GT2006-90453

[14] Gentilhomme, O., Hills, N. J., Turner, A. B., and Chew, J. W., 2003, "Measurement and Analysis of Ingestion Through a Turbine Rim Seal," ASME J. Turbomach, 125(3), pp. 505-512.

[15] Bohn, D., and Wolff, M., 2003, "Improved Formulation to Determine Minimum Sealing Flow: *Cw, min* - for Different Sealing Configurations," ASME Paper GT2003-38465.

[16] Johnson, B.V., Jakoby, R., Bohn, D.E. and Cunat, D., 2009, “A Method for Estimating the Influence of Time-Dependent Vane and Blade Pressure Fields on Turbine Rim Seal Ingestion”; ASME J.Turbomach., Vol. 131, Issue 2, 021005-1 to 10.

[17] Bohn, D. E., Decker, A., Ma, H., and Wolff, M., 2003, "Influence of Sealing Air Mass Flow on the Velocity Distribution in and Inside the Rim of the Upstream Cavity of a 1.5-Stage Turbine," ASME Paper GT2003-38459.

[18] Johnson, B. V., Wang, C. Z., and Roy, R. P., 2008, "A Rim Seal Orifice Model with 2 Cd s and Effects of Swirl in Seals," ASME Paper GT2008-50650.

[19] Zhou, K., Wilson, M., Lock, G. D., and Owen, J. M., 2011, "Computation of Ingestion through Gas Turbine Rim Seals," ASME Paper GT2011-45314.

[20] Zhou, K., Wood, S. N., and Owen, J. M., 2011, "Statistical and Theoretical Models of Ingestion through Turbine Rim Seals," ASME Paper GT2011-45139.

[21] Owen, J. M., and Rogers, R. H., 1989, Flow and Heat Transfer in Rotating-Disc Systems, Volume 1 - Rotor Stator Systems. Research Studies Press Ltd, Taunton, UK.